ADVANCED FUNCTIONAL MATERIALS
www.afm-journal.de

Materials Views
www.MaterialsViews.com

Ultrasmall Sn Nanoparticles Embedded in Carbon as High-Performance Anode for Sodium-Ion Batteries

Yongchang Liu, Ning Zhang, Lifang Jiao, Zhanliang Tao, and Jun Chen**

Designed as a high-capacity, high-rate, and long-cycle life anode for sodium-ion batteries, ultrasmall Sn nanoparticles (≈8 nm) homogeneously embedded in spherical carbon network (denoted as 8-Sn@C) is prepared using an aerosol spray pyrolysis method. Instrumental analyses show that 8-Sn@C nanocomposite with 46 wt% Sn and a BET surface area of 150.43 $m^2 g^{-1}$ delivers an initial reversible capacity of ≈493.6 mA h g^{-1} at the current density of 200 mA g^{-1}, a high-rate capacity of 349 mA h g^{-1} even at 4000 mA g^{-1}, and a stable capacity of ≈415 mA h g^{-1} after 500 cycles at 1000 mA g^{-1}. The remarkable electrochemical performance of 8-Sn@C is owing to the synergetic effects between the well-dispersed ultrasmall Sn nanoparticles and the conductive carbon network. This unique structure of very-fine Sn nanoparticles embedded in the porous carbon network can effectively suppress the volume fluctuation and particle aggregation of tin during prolonged sodiation/desodiation process, thus solving the major problems of pulverization, loss of electrical contact and low utilization rate facing Sn anode.

1. Introduction

Sodium-ion batteries (SIBs) as an alternative to lithium-ion batteries (LIBs) have attracted increasing attention owing to the natural abundance of sodium.[1] The low cost and huge availability of Na compounds give SIBs a potential advantage in large-scale energy storage applications.[2] Although the intercalation mechanism of Na in electrode materials is similar to that of Li, the larger size of Na^+ ion (1.02 Å in radius) as compared to Li^+ ion (0.59 Å in radius) makes it difficult to simply adopt the recent strategies proposed for high-performance LIBs.[3] The key challenge facing SIBs is to develop appropriate host materials with the capability for fast and stable sodium-ion insertion/extraction.[4] Particularly, only few of Na-storage anode materials have demonstrated suitable redox capacity and adequate cyclability.[5] As known, graphite is a well-accepted Li-storage anode, but it fails to intercalate sodium effectively, presumably because of the mismatching of graphite interlayer distance (d_{002} = 0.334 nm) with the larger Na^+ ions.[6] Si-based material is expected as a next-generation anode for LIBs but not in SIB systems. This is because Si cannot incorporate sodium ions like in case of lithium ions.[4,7] Until now, Na-storage anode materials have been explored, mainly including metals and alloys (e.g., Sn, Sb, Ge, SnSb and SnSbGe),[8,9] metal oxides/sulfides,[10] carbonaceous materials and their composites.[11] Among them, Sn is a promising anode material due to its high theoretical capacity (847 mA h g^{-1} with $Na_{15}Sn_4$), low cost, environmental friendliness, and appropriate low charge–discharge potentials versus Na/Na^+. Nevertheless, a 520% volume expansion from Sn to $Na_{15}Sn_4$ would essentially prevent the access of high capacity.[6] During electrochemical cycling, this enormous volume change will lead to a continuous pulverization of electrode materials and then a rapid deterioration of the cyclability,[8] as the case in LIBs.[12] To solve this problem, a number of techniques were adopted to buffer the volume fluctuation. For example, sponge-like porous C/Sn composite was reported with a capacity of ≈200 mA h g^{-1} for 15 cycles at 20 mA g^{-1}.[13] Then, three dimensional (3D) array of Sn nanorods was fabricated with an initial capacity of 722 mA h g^{-1} and a ≈60% capacity retention after 150 cycles at 50 mA g^{-1}.[14] In comparison, Sn@native wood fiber composite was also developed, which delivers an initial capacity of 339 mA h g^{-1} with ≈43% capacity retention over 400 cycles at 84 mA g^{-1}.[15] These ways indeed improved the ability of sodium ion storage in Sn anode, but the performance was still far away from meeting low-cost and large-scale applications. To date, a high-capacity Sn anode with high-rate capability and long-cycle life for SIBs has yet to be identified. Considerable improvements in the design and optimization of anode composition and structure are still required.

Throughout the extensive strategies, which have been applied to enhance the electrochemical behavior of Sn anode in both LIBs and SIBs, it is found that reducing the particle size of Sn to nanoscale (especially within 10 nm) can endure much higher strain and effectively mitigate the pulverization

Dr. Y. Liu, Dr. N. Zhang, Prof. L. Jiao, Prof. Z. Tao, Prof. J. Chen
Key Laboratory of Advanced Energy Materials Chemistry (Ministry of Education)
Collaborative Innovation Center of Chemical Science and Engineering (Tianjin)
College of Chemistry, Nankai University
Tianjin 300071, China
E-mail: jiaolf@nankai.edu.cn; chenabc@nankai.edu.cn

DOI: 10.1002/adfm.201402943

of the active materials.[16,17] Nevertheless, nanosized particles tend to aggregate during the electrochemical alloying-dealloying process, resulting in an inevitable capacity decay.[18] Correspondingly, integrating nano-Sn with a conductive matrix such as carbon, can dilute the opportunities for Sn aggregation and accommodate volume expansion for keeping the integrity of the electrode.[19,20] Specifically, Wang's group successfully fabricated nano-Sn/C composite with the Sn particle size of ≈10 nm.[17] Our group also synthesized nitrogen-doped porous C/Sn (≈5 nm) and pitaya-like Sn (≈8 nm) @C nanocomposites.[18,19] These distinctive structures exhibit high reversible capacity as well as good cyclic stability in LIB applications owing to the ultrasmall size and uniform distribution of Sn nanoparticles (NPs). To the best of our knowledge, since the design of ultrasmall-Sn@C has not been reported in Na-storage and, furthermore, since both ultrasmall tin with large specific surface area is readily accessible to the electrolyte and conductive carbon framework is identified to facilitate the Na^+ ions diffusion,[11] here we report on the preparation of ultrasmall Sn NPs (with typical size of ≈8 nm) finely embedded in spherical carbon network (denoted as 8-Sn@C) by aerosol spray pyrolysis and its application as anode material for sodium-ion batteries with superior electrochemical performance.

2. Results and Discussion

The preparation details are provided in the Experimental Section and Figure S1 (Supporting Information). Briefly, $SnCl_2 \cdot 2H_2O$ and resorcinol formaldehyde (RF) resin, which acted as tin and carbon sources, respectively, were dissolved into ethanol to form a precursor solution. The resorcinol formaldehyde resin is a low-cost carbon provider with negative charges, which can effectively coat Sn^{2+} surface. During the spraying by constant output atomizer, the precursor solution generated small droplets continuously, then RF resin was carbonized. Simultaneously, Sn^{2+} was reduced in an inert atmosphere furnace (800 °C) within 1–2 s. In traditional syntheses, it is hard to shorten the heating time to second level and inevitably sinter the Sn nucleus. In our method, the short residence time and rapid subsequent cooling enable the produced Sn grains to keep nanosized and distribute uniformly in a carbon matrix. For comparison, spherical Sn@C composite with ≈50 nm diameter of embedded Sn grains (denoted as 50-Sn@C) was also obtained by changing the mass ratio of tin and carbon sources.

Figure 1a shows the X-ray diffraction (XRD) patterns of as-prepared pure metallic Sn, 50-Sn@C, and 8-Sn@C composites by aerosol spray pyrolysis. All the diffraction peaks could be

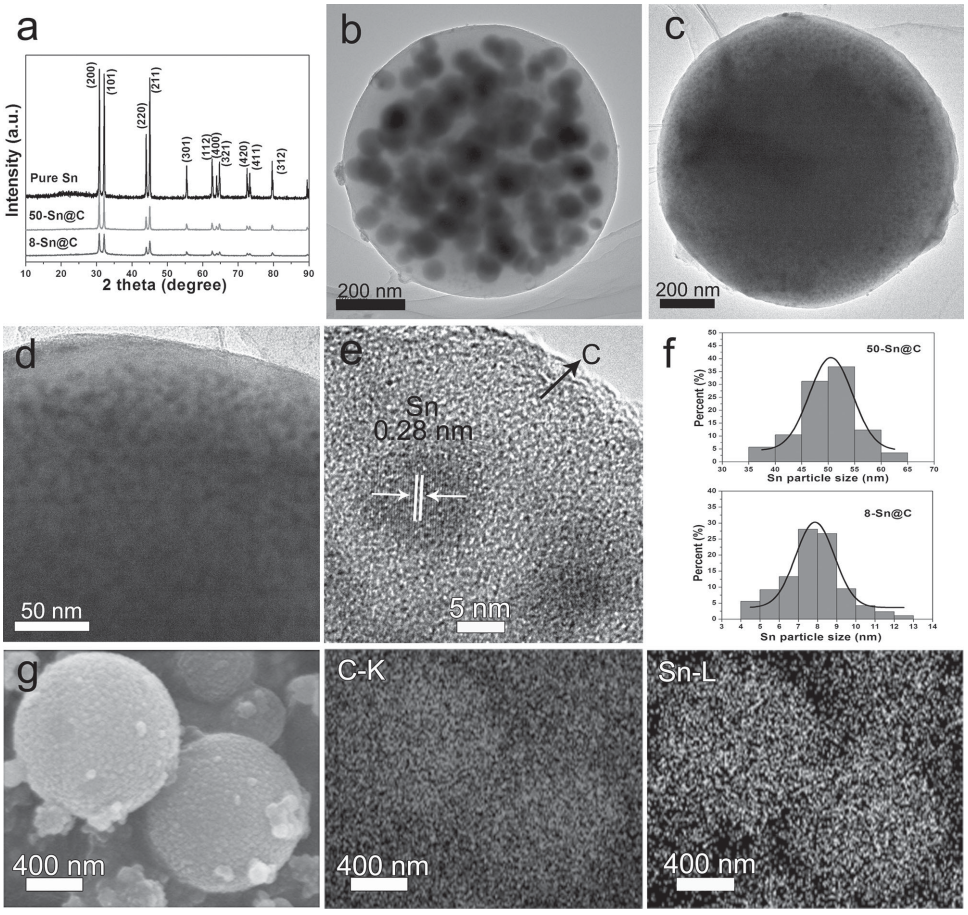

Figure 1. a) XRD patterns of the as-prepared pure metallic Sn, 50-Sn@C, and 8-Sn@C nanocomposites. b) TEM image of 50-Sn@C, c) TEM image and d,e) HRTEM images of 8-Sn@C. f) Sn particle size distribution diagrams of the two composites. g) SEM and EDS mapping images of 8-Sn@C.

readily indexed to the tetragonal tin (JCPDS card no. 04–0673), while no peaks of impurities are detected. Moreover, the notably shortened and broadened peaks of the composites relative to pure Sn demonstrate the much smaller Sn particle-size of 50-Sn@C and 8-Sn@C.[21] No intensive peak belonging to carbon is detected, demonstrating the amorphous nature of carbon.[18] This is supported by the Raman spectra of the two Sn@C samples (Figure S2, Supporting Information), in which two broad peaks at 1346 and 1585 cm^{-1} can be assigned to typical D and G bands of amorphous carbon, respectively.[22] The XRD pattern of pyrolyzed carbon with characteristic (002) and (100) peaks is displayed in Figure S3 (Supporting Information). Figure 1b,c presents the transmission electron microscopy (TEM) images of the two composites. It can be seen that 50-Sn@C and 8-Sn@C both exhibit sphere-like architecture with Sn nanoparticles (black dots) embedded in carbon (grey color) matrix. Differently, the high-resolution TEM (HRTEM) image in Figure 1d and the particle size distribution diagrams in Figure 1f (by measuring 100 Sn nanoparticles using Nano-Measure software) indicate that the tin grains in 8-Sn@C are around 8 nm and dispersed homogeneously in carbon matrix; while the Sn particles in 50-Sn@C are ~50 nm with some aggregation. The optimum concentration of 8-Sn@C precursor solution and the stable carbon frame can effectively prevent Sn nanograins from growing bigger.[17] Furthermore, the rapid formation of Sn@C network at high reaction temperature is considered to protect the uniform distribution of Sn nanoparticles.[19] Figure 1e shows a set of parallel fringes with the space of 0.28 nm, corresponding to the (101) plane of crystalline Sn.[23] Figure 1g shows the scanning electron microscopy (SEM) image and the energy dispersive spectrometer (EDS) mapping of 8-Sn@C, revealing a homogeneous distribution of Sn within the carbon framework. The large scale SEM images of 8-Sn@C and 50-Sn@C composites are displayed in Figure S4 (Supporting Information). From which, it can be seen that the size of spherical 50-Sn@C is mainly in the range of 0.4–1.5 μm, relatively larger than that of 8-Sn@C (0.2–1.0 μm).

The composition of the spherical Sn@C nanocomposite was investigated by thermogravimetric analysis (TGA) in air, as shown in Figure S5 (Supporting Information). The only 2% weight loss observed until 220 °C is attributed to the elimination of adsorbed water. This suggests that the composite is stable in air up to 220 °C. The weight increase in the temperature range of 220 °C to 300 °C or around 350 °C is owing to the oxidation of metallic tin ($Sn + O_2 \rightarrow SnO_2$). The fast weight loss until 550 °C is assigned to the carbon decomposition ($C + O_2 \rightarrow CO_2$ (gas)). As can be calculated, the mass contents of tin in 8-Sn@C and 50-Sn@C composites are approximately 46% and 74%, respectively.

Figure 2 shows the N_2 adsorption-desorption isotherms and pore size distribution curves of the Sn@C composites. The isotherms with a steep increase at relatively high pressure ($P/P_0 > 0.6$) is typical type-IV behavior (Figure 2a), implying that the composites contain a large amount of mesopores, which are resulted from gas volatilization during the carbonization

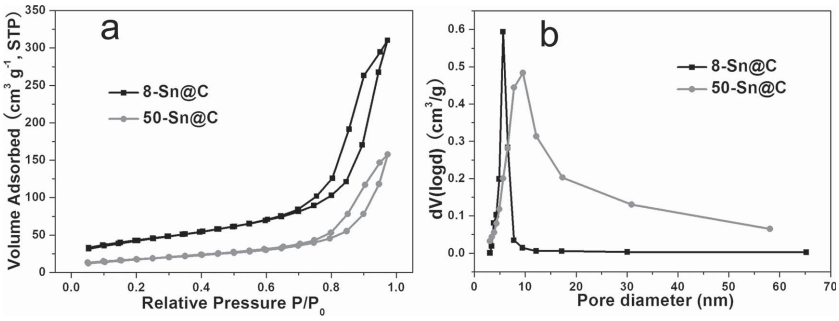

Figure 2. a) N_2 adsorption-desorption isotherms and b) BJH pore size distribution plots of 8-Sn@C and 50-Sn@C composites.

of RF resin along with the pyrolysis of $SnCl_2 \cdot 2H_2O$. Accordingly, 8-Sn@C possesses a large BET specific surface area of 150.43 $m^2\ g^{-1}$, while the surface area of 50-Sn@C is only 60.17 $m^2\ g^{-1}$. The highly dispersed ultrasmall Sn NPs of 8-Sn@C contributes to the larger surface area. From Figure 2b, it can be seen the BJH pore size of 8-Sn@C is in the range of 5–8 nm, while it is 5–20 nm for 50-Sn@C.

The electrochemical reactivity of 8-Sn@C nanocomposite was evaluated by cyclic voltammograms (CVs, **Figure 3**a). The first cathodic scan shows a wide current peak in the range of 0.1 to 0.8 V versus Na/Na^+, corresponding to the formation of solid-electrolyte interface (SEI) film and Na_xSn alloy.[13] The peaks located at 0.35 and 0.18 V in subsequent cathodic scans are intrinsically attributed to the sodiation process.[14] In the anodic scans, four well-defined peaks at 0.22, 0.30, 0.58 and 0.70 V are assigned to the desodiation of $Na_{15}Sn_4$, Na_9Sn_4, NaSn, and $NaSn_5$, respectively. These desodiation potentials are in good agreement with the calculated and experimental results of Sn anode reported previously.[4,8,14] Moreover, a small cathodic peak near 0.05 V and a counterpart anodic peak at 0.12 V are observed, resembling the cycle voltammetry behavior of sodium insertion/extraction in carbon (Figure S6, Supporting Information).[11] The overall reaction process of Sn@C composite in SIBs can be described as Equations 1,2:

$$4Sn + 15Na^+ + 15e^- \leftrightarrow Na_{15}Sn_4 \quad (1)$$

$$xC + Na^+ + e^- \leftrightarrow NaC_x \quad (2)$$

Figure 3b displays the first four galvanostatic charge–discharge profiles of 8-Sn@C electrode at a current density of 200 mA g^{-1}. In consist with the above CV study, two inconspicuous plateaus appeared at 0.35 and 0.20 V in the discharge curves correspond to the sodiation process. In the charge profiles, two potential plateaus are presented at 0.25 and 0.65 V, which is characteristic of stepwise dealloying $Na_{15}Sn_4$. The adjacent desodiation processes appeared in CV curves (0.22 and 0.30 V, 0.58 and 0.70 V) merge into one charge plateau, this is in great consistent with previous reports.[13–15,22] It is worth mentioning that the desodiation potentials of Na_xSn are much lower than the delithiation potentials of Li_xSn (0.6–0.9 V vs Li/Li^+),[18] implying that Sn is a more appropriate anode material for Na-ion storage. In addition, the first discharge and charge capacities are 736.7 mA h g^{-1} and 493.6 mA h g^{-1}, respectively,

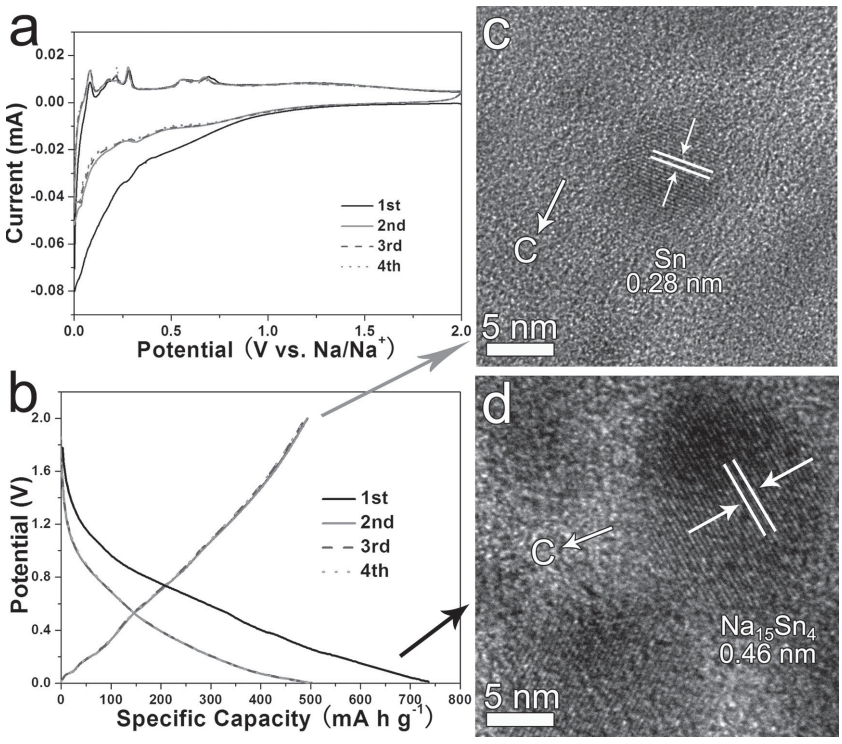

Figure 3. a) Cyclic voltammetry curves of 8-Sn@C electrode at 0.05 mV s^{-1} scanning rate. b) Galvanostatic charge–discharge profiles of 8-Sn@C electrode between 0.01 and 2.0 V vs Na/Na^+ at a constant current density of 200 mA g^{-1}. c) HRTEM images of 8-Sn@C nanocomposite after first charge and d) discharge process.

corresponding to a Coulombic efficiency (CE) of 67%. The capacity loss of 243 mA h g^{-1} in the first cycle is mainly attributed to the formation of SEI film. It should be noted that from the second cycle, either the discharge or charge curves are well overlapped, indicating the high capacity retention of 8-Sn@C electrode.

Figure 3c,d shows the ex situ HRTEM images of the reaction products after the first charge/discharge (8-Sn@C electrode charged to 2.0 V vs Na/Na^+, discharged to 0.01 V vs Na/Na^+). It can be clearly seen that the discharge product is well attributed to $Na_{15}Sn_4$ alloy with the (101) interplanar spacing of 0.46 nm. The size of $Na_{15}Sn_4$ NPs is around 7–13 nm, confirming that ultrasmall Sn embedded in carbon matrix can effectively suppress the volume expansion during sodiation.[24] After desodiation, $Na_{15}Sn_4$ alloy recovers to Sn NPs, showing lattice fringes with the distance of 0.28 nm. The above observations demonstrate the reversible reaction mechanism through electrochemical conversion of Equation 1, which is in agreement with previous test using in situ XRD.[8]

Figure 4a depicts the rate capability and cycling performance of the as-synthesized Sn@C composites. It can be found that 8-Sn@C electrode not only fully utilizes the ultrasmall Sn NPs to store sodium ions with high capacity (even at high current densities), but also improves the cyclic stability. In the initial cycles, it delivers a reversible capacity as high as 493.6 mA h g^{-1} at the current density of 200 mA g^{-1}. After 20 cycles, the current rate is gradually increased with a few cycles at 500, 1000, 2000, and 4000 mA g^{-1}. The corresponding reversible capacities can reach 447, 420, 388, and 349 mA h g^{-1}, respectively. The ultrasmall Sn nanoparticles (≈8 nm) with large specific surface area are readily accessible to the electrolyte. This high porosity and high electrical conductivity of the whole framework would fasten the reversible insertion/extraction of Na^+ ions,[25] which is favorable for the high-rate capability. More importantly, when the current density is brought down to 200 mA g^{-1} after such high current cycling, the desodiation capacity swiftly recovers to 492 mA h g^{-1} within few cycles. The cell is further tested at a high current density of 500 mA g^{-1} to 200 cycles, the obtained capacity remains stable at ≈445 mA h g^{-1} with negligible fading. By contrast, the 50-Sn@C electrode exhibits an inferior rate capability with much poor cycling performance. The maximum desodiation capacities obtained at 200, 500, 1000, 2000, and 4000 mA g^{-1} are 506, 309, 225, 134, and 64 mA h g^{-1}, respectively. After 60 cycles, when the current rate is back to 200 mA g^{-1}, just 70.9% of the initial capacity is retained. During the subsequent cycling at 500 mA g^{-1}, only a low capacity of ≈215 mA h g^{-1} can be obtained over 200 cycles.

For the evaluation of the long-term cycle stability of 8-Sn@C electrode, the electrode was galvanostatically discharged and charged at 1000 mA g^{-1} for 500 cycles (Figure 4b). The reversible capacities at the end of 20, 100, 200, 300, 400, and 500 cycles were 425 mA h g^{-1}, 411 mA h g^{-1}, 418 mA h g^{-1}, 410 mA h g^{-1}, 419 mA h g^{-1}, and 415 mA h g^{-1}, respectively. There was practically no capacity decrease over the five hundred cycles even at such a high rate. Remarkably, the Coulombic efficiency approaches 100% (>99.5%), implying that the superior cycle stability of 8-Sn@C electrode for reversible Na^+ storage was highly repeatable. The excellent electrochemical performance of 8-Sn@C compares favorably with that of previously reported Sn anodes for SIBs (**Table 1**).[13–15,22,26–28]

Furthermore, the morphological and structural changes of the Sn@C electrodes after high-rate and long-time cycling

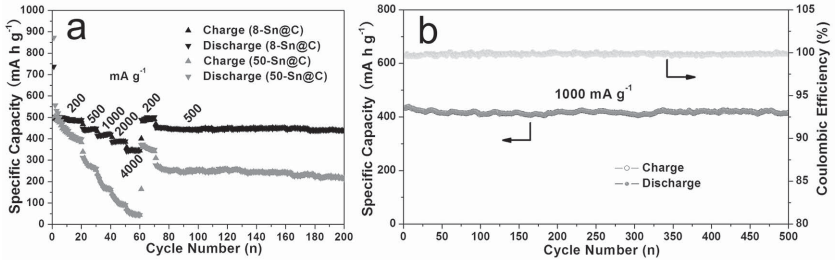

Figure 4. a) Rate capability and cycling performance of the 8-Sn@C and 50-Sn@C electrodes in the voltage range of 0.01 to 2.0 V. b) Long-term cycle stability of the 8-Sn@C electrode at a current density of 1000 mA g^{-1}.

Table 1. Comparison of the results in this study with previously reported performance of Sn anodes for SIBs.

Sample	Rate capability	Cyclic stability	Ref.
Porous C/Sn	–	≈200 mA h g^{-1} at 20 mA g^{-1} (15 cycles)	[13]
C/Sn/Ni/TMV	–	405 mA h g^{-1} at 50 mA g^{-1} (150 cycles)	[14]
Sn@Wood fiber	–	145 mA h g^{-1} at 84 mA g^{-1} (400 cycles)	[15]
Al_2O_3/Sn@CNF	–	650 mA h g^{-1} at 84.7 mA g^{-1} (40 cycles)	[22]
$Sn_{0.9}Cu_{0.1}$	265 mA h g^{-1} at 424 mA g^{-1} 182 mA h g^{-1} at 847 mA g^{-1} 126 mA h g^{-1} at 1694 mA g^{-1}	≈420 mA h g^{-1} at 169 mA g^{-1} (100 cycles)	[26]
Sn-polyacrylate	–	≈500 mA h g^{-1} at 50 mA g^{-1} (25 cycles)	[27]
Sn/graphite composite	–	≈350 mA h g^{-1} at 50 mA g^{-1} (20 cycles)	[28]
8-Sn@C	493 mA h g^{-1} at 200 mA g^{-1} 447 mA h g^{-1} at 500 mA g^{-1} 420 mA h g^{-1} at 1000 mA g^{-1} 388 mA h g^{-1} at 2000 mA g^{-1} 349 mA h g^{-1} at 4000 mA g^{-1}	440 mA h g^{-1} at 500 mA g^{-1} (200 cycles) 415 mA h g^{-1} at 1000 mA g^{-1} (500 cycles)	Present work

were examined using TEM. As revealed in **Figure 5**a, the fresh spherical 50-Sn@C composite was collapsed to some extent after 200 cycles and partial Sn grains pulverized with aggregation. This should account for the rapid capacity decay of 50-Sn@C. On the contrary, Figure 5,c manifests that 8-Sn@C anode still retains its original appearance over 200 cycles. Notably, all Sn NPs with little volume expansion are uniformly confined in the spherical carbon matrix, certifying that the unique structure effectively alleviates the pulverization and aggregation of metallic tin particles, thus maintaining the integrity of the whole electrode and ensuring the long-cycle life. In addition, SEM and EDS mapping images of the cycled 8-Sn@C (Figure 5d) further clarify the homogeneous distribution of Sn throughout the whole carbon network. After optimization of the electrochemical performance of C, 8-Sn@C, 50-Sn@C, and Sn (Figure S7 and Table S1, Supporting Information), it is shown that pure carbon contributes about 200 mA h g^{-1} at 200 mA g^{-1}. Thus, a reversible capacity of ≈493 mA h g^{-1} is reasonable for 8-Sn@C composite (with 54 wt% carbon and 46 wt% tin).

The electrochemical impendence spectra (EIS) of the two Sn@C composites are compared in Figure S8 and Table S2 (Supporting Information). As can be seen, the 8-Sn@C electrode shows a much lower charge-transfer resistance than that of the 50-Sn@C electrode (47.8 Ω vs 138 Ω) on the basis of the equivalent circuit given in the inset. Hence the exchange current densities ($i^\circ = RT/nFR_{ct}$) of the cell based on 8-Sn@C are higher than those of 50-Sn@C. The fast charge-transfer kinetics of 8-Sn@C electrode indicates that the smaller Sn grains homogeneously distributed in conductive carbon could facilitate sodium-ion diffusion. In general, the superior electrochemical performance of 8-Sn@C is attributed to three main reasons. First, the ultrasmall Sn NPs (≈8 nm) can significantly reduce the absolute strain and improve the utilization rate of active materials during sodiation/desodiation process. Second, the carbon frame can accommodate the large volume fluctuation and bring a strong buffering effect to prevent metal aggregation over repeated cycling. Third, the uniform distribution of Sn

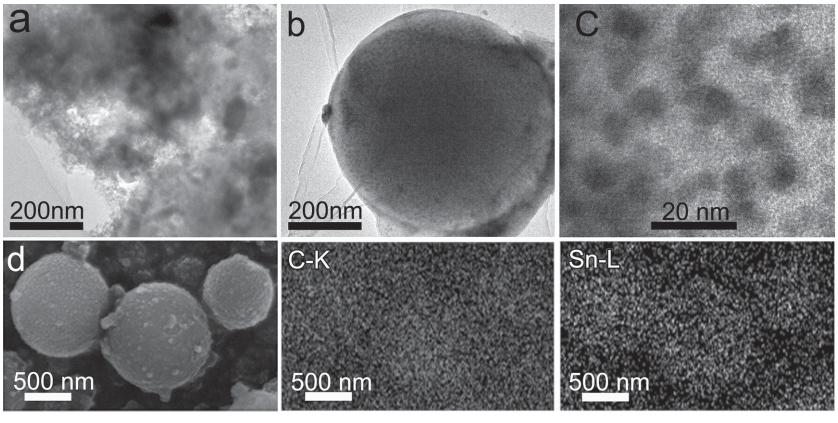

Figure 5. TEM images of a) 50-Sn@C composite and b,c) 8-Sn@C composite after 200 charge/discharge cycles. d) SEM and EDS mapping images of 8-Sn@C after 200 cycles.

NPs in the carbon matrix is an important factor to generate a balanced stress over the whole composite and electrode, thus enhancing long-term performance.

3. Conclusion

In conclusion, Sn@C composite with ultrasmall Sn nanoparticles (≈8 nm) homogeneously dispersed in spherical carbon network was prepared by aerosol spray pyrolysis and further evaluated as anode material for rechargeable Na-ion batteries. The unique structure with very fine Sn nanoparticles embedded in the carbon network can effectively alleviate the expansion/contraction stress, accommodate the large volume changes during the insertion/extraction, and prevent the pulverization and agglomeration of Sn grains upon prolonged cycling. Consequently, 8-Sn@C electrode delivered a reversible capacity as high as ≈493.6 mA h g^{-1} at the current density of 200 mA g^{-1}. Moreover, the capacity of 349 mA h g^{-1} even at 4000 mA g^{-1} and ≈415 mA h g^{-1} over 500 cycles at 1000 mA g^{-1} were obtained, showing high-rate capability and long cycling life of 8-Sn@C. This result should provide the basis for the potential application of Sn-based materials as high-performance anode for sodium-ion batteries.

4. Experimental Section

Materials Synthesis: After optimization of the mass ratio of Sn and carbon (Figure S9, Supporting Information), spherical Sn@C nanocomposite with Sn NPs of ≈8 nm (8-Sn@C) was prepared by an aerosol spray pyrolysis technique. In the typical synthesis, 6.8 g (0.1 mol L^{-1}) $SnCl_2{\cdot}2H_2O$ (Sigma-Aldrich, 99%), 7.7 g resorcinol (Acros, 99%) and 10 mL formaldehyde (Acros, 98%) were dissolved into 290 mL ethanol to form a homogeneous clear solution. The precursor solution was sprayed with argon flow using a constant output atomizer (Model 3076, TSI, Inc.) under the gauge pressure of 0.2 MPa. The aerosols subsequently passed through a cannular reactor (2.54 cm (ID) × 80 cm (L)) within tubular furnace at 800 °C for residence time about 1–2 s. In this case, $SnCl_2$ was decomposed to Sn under the Ar environment at high temperature, and the generated Sn grains function as catalysts to promote the formation of carbon. While the carbon frame and the short residence time in the furnace restrict the growth of Sn grains, thus forming an uniform ultrasmall-Sn@C composite. The final product was collected on a small quartz tube (2.5 cm (ID) × 2.0 cm (L)),which was placed at the end of the reactor. For comparison, spherical Sn@C composite with ≈50 nm diameter of Sn nanoparticles (designated as 50-Sn@C) was obtained by just altering the dosage of $SnCl_2{\cdot}2H_2O$, resorcinol, formaldehyde and ethanol to 33.8 g (0.5 mol L^{-1}), 7.7 g, 10 mL and 290 mL, respectively. Pure metallic Sn was fabricated by heating the sprayed droplets of $SnCl_2{\cdot}2H_2O$/ethanol precursor solution (0.1 mol L^{-1}) at 800 °C. The pyrolyzed carbon without Sn was synthesized as following steps: 7.7 g resorcinol and 10 mL formaldehyde were prepolymerized in advance to form a clear solution at 298 K. After 60 min stirring, the solution was carbonized with a heating rate of 5 °C min^{-1} in flowing argon at 800 °C for 30 min.

Materials Characterizations: X-ray diffraction (XRD) analysis was performed on a Rigaku D/Max-2500 with Cu-Kα radiation (λ = 1.54178 Å). The 2θ angular region between 10° and 90° was investigated at a scan rate of 4° min^{-1}. The morphology and microstructure were observed by field-emission scanning electron microscopy (SEM, JEOL JSM7500F) and transmission electron microscopy (TEM, Philips Tecnai-F20). N_2 adsorption-desorption isotherms were measured with Quantachrome Instruments (NoVA 2200e) and the N_2 desorption temperature was 300 °C. The surface areas were calculated by the Brunauere-Emmette-Teller (BET) method and the pore size distributions were obtained from the adsorption branches of the isotherms using the Barrette-Joynere-Halenda (BJH) method. Thermogravimetric analysis (TGA) was carried out to test the carbon contents of spherical Sn@C composites using a TG-DSC analyzer (NETZSCH, STA 449 F3) with a heating rate of 5 °C min^{-1} in air from room temperature to 700 °C. Assuming that only SnO_2 would remain after all the carbon being oxidized into gaseous CO_2 after TGA experiment, the Sn content could be calculated based on the following equation:

$$\mathrm{Sn(wt\%)} = 100 \times \frac{\text{molecular weight of Sn}}{\text{molecular weight of } SnO_2} \times \frac{\text{final weight}}{\text{initial weight}} \quad (3)$$

Electrochemical Measurements: The Sn@C electrode was fabricated by mixing 70 wt% active materials, 15 wt% super P carbon, and 15 wt% carboxymethyl cellulose (CMC) binder in distilled water solvent to form homogeneous slurry. The mixture was coated onto copper foil. The coated electrode was dried at 80 °C for 12 h in a vacuum oven and then pressed. The active material loading was about 1.5–2.0 mg cm^{-2} without deducting the mass of carbon. Electrochemical tests were carried out using CR2032 coin cells assembled in an argon-filled glove box with water and oxygen contents below 5 ppm. The counter/reference electrode was sodium metal, and the separator was glass fiber. The electrolyte solution was 1 M $NaClO_4$ dissolved in ethylene carbonate/diethyl carbonate (EC/DEC, 1:1 in volume). Galvanostatic discharge/charge tests were performed in the voltage range of 0.01–2.0 V at different rates on a LAND battery-test instrument (CT2001A). The applied current densities are based on the mass of whole Sn@C composites. Cyclic voltammetry was conducted on a CHI660B electrochemical workstation at a scan rate of 0.05 mV s^{-1} within a potential window of 0.01–2.0 V. Electrochemical impedance spectra (EIS, Zahner IM6ex) were obtained by applying a sine wave with amplitude of 5.0 mV over the frequency range from 100 kHz to 100 mHz. Before EIS tests, the assembled cells were first discharged/charged at a current density of 200 mA g^{-1} for 5 cycles to stabilize the cells. All the tests were performed at 298 K. When investigating the cycled active materials using TEM or SEM, the electrode slice was taken out from the cells in an argon-filled glove box. Then the electrode was washed with diethyl carbonate (DEC) for several times and subsequently sonicated in ethanol to prepare the testing samples.

Supporting Information

Supporting Information is available from the Wiley Online Library or from the author.

Acknowledgements

This work was supported by Programs of 973 (2011CB935900), NSFC (21322101), and MOE (B12015 and IRT13R30).

Received: August 26, 2014
Revised: October 2, 2014
Published online: October 27, 2014

[1] a) B. Dunn, H. Kamath, J. M. Tarascon, *Science* **2011**, *334*, 928; b) K. Sakaushi, E. Hosona, G. Nickerl, T. Gemming, H. Zhou, S. Kaskel, J. Eckert, *Nat. Commun.* **2013**, *4*, 1485; c) B. L. Ellis, L. F. Nazar, *Curr. Opin. Solid State Mater. Sci.* **2012**, *16*, 168; d) M. D. Slater, D. Kim, E. Lee, C. S. Johnson, *Adv. Funct. Mater.* **2013**, *23*, 947; e) S. Xin, Y. X. Yin, Y. G. Guo, L. J. Wan, *Adv. Mater.* **2014**, *26*, 1261.

[2] a) C. D. Wessells, S. V. Peddada, R. A. Huggins, Y. Cui, *Nano Lett.* **2011**, *11*, 5421; b) S. W. Kim, D. H. Seo, X. H. Ma, G. Ceder, K. Kang, *Adv. Energy Mater.* **2012**, *2*, 710; c) V. Palomares, P. Serras, I. Villaluenga, K. B. Hueso, J. G. Gonzalez, T. Rojo, *Energy Environ. Sci.* **2012**, *5*, 5884; d) N. Yabuuchi, M. Kajiyama, J. Iwatate, H. Nishikawa, S. Hitomi, R. Okuyama, R. Usui, Y. Yamada, S. Komaba, *Nat. Mater.* **2012**, *11*, 512; e) S. W. Wang, L. J. Wang, Z. Q. Zhu, Z. Hu, Q. Zhao, J. Chen, *Angew. Chem. Int. Ed.* **2014**, *53*, 5892.

[3] a) C. Zhu, X. Mu, P. A. van Aken, Y. Yu, J. Maier, *Angew. Chem. Int. Ed.* **2014**, *53*, 2152; b) Z. Hu, L. Wang, K. Zhang, J. Wang, F. Y. Cheng, Z. L. Tao, J. Chen, *Angew. Chem.* **2014**, DOI: 10.1002/ange.201407898; c) Y. U. Park, D. H. Seo, H. S. Kwon, B. Kim, J. Kim, H. Kim, I. Kim, H. L. Yoo, K. Kang, *J. Am. Chem. Soc.* **2013**, *135*, 13870.

[4] V. L. Chevrier, G. Ceder, *J. Electrochem. Soc.* **2011**, *158*, A1011.

[5] a) P. Sengutturan, G. Rousse, M. E. Arroyo y de Dompablo, H. Vezin, J. M. Tarascon, M. R. Palacin, *J. Am. Chem. Soc.* **2013**, *135*, 3897; b) W. Li, S. L. Chou, J. Z. Wang, J. H. Kim, H. K. Liu, S. X. Dou, *Adv. Mater.* **2014**, *26*, 4037.

[6] J. F. Qian, Y. Xiang, Y. L. Cao, X. P. Ai, H. X. Yang, *Nano Lett.* **2014**, *14*, 1865.

[7] H. Ma, F. Y. Cheng, J. Chen, J. Zhao, C. S. Li, Z. L. Tao, J. Liang, *Adv. Mater.* **2007**, *19*, 4067.

[8] L. D. Ellis, T. D. Hatchard, M. N. Obrovac, *J. Electrochem. Soc.* **2012**, *159*, A1801.

[9] a) A. Darwiche, C. Marino, M. T. Souugrati, B. Fraisse, L. Stierano, L. Monconduit, *J. Am. Chem. Soc.* **2012**, *134*, 20805; b) P. R. Abel, Y. M. Lin, T. D. Souza, C. Y. Chou, A. Gupta, J. B. Goodenough, G. S. Hwang, A. Heller, C. B. Mullins, *J. Phys. Chem. C* **2013**, *117*, 18885; c) L. W. Ji, M. Gu, Y. Y. Shao, X. L. Li, M. H. Engelhard, B. W. Arey, W. Wang, Z. M. Nie, J. Xiao, C. M. Wang, J. G. Zhang, J. Liu, *Adv. Mater.* **2014**, *26*, 2901; d) B. Farbod, K. Cui, W. P. Kalisvaart, M. Kupsta, B. Zahiri, A. Kohandehghan, E. M. Lotfabd, Z. Li, E. J. Luber, D. Mitlin, *ACS Nano* **2014**, *8*, 4415.

[10] a) Y. Cao, L. Xiao, W. Wang, D. Choi, Z. Nie, J. Yu, L. V. Saraf, Z. Yang, J. Liu, *Adv. Mater.* **2011**, *23*, 3155; b) Y. Wang, X. Yu, S. Xu, J. Bai, R. Xiao, Y. S. Hu, H. Li, X. Q. Yang, L. Chen, X. Huang, *Nat. Commun.* **2013**, *4*, 2365; c) D. W. Su, H. J. Ahn, G. X. Wang, *Chem. Commun.* **2013**, *49*, 3131; d) Z. Jian, B. Zhao, P. Liu, F. Li, M. Zheng, M. Chen, Y. Shi, H. Zhou, *Chem. Commun.* **2014**, *50*, 1215; e) L. J. Wang, K. Zhang, Z. Hu, W. C. Duan, F. Y. Cheng, J. Chen, *Nano Res.* **2014**, *7*, 199; f) B. H. Qu, C. Z. Ma, G. Ji, C. H. Xu, J. Xu, Y. S. Meng, T. H. Wang, J. Y. Lee, *Adv. Mater.* **2014**, *26*, 3854.

[11] a) S. Komaba, W. Murata, T. Ishikawa, N. Yabuuchi, T. Ozeki, T. Nakayama, A. Ogata, K. Gotoh, K. Fujiwara, *Adv. Funct. Mater.* **2011**, *21*, 3859; b) K. Tang, L. Fu, R. J. White, L. Yu, M. M. Titirici, M. Antonietti, J. Maier, *Adv. Energy Mater.* **2012**, *2*, 873; c) J. Ding, H. L. Wang, Z. Li, A. Kohandehghan, K. Cui, Z. W. Xu, B. Zahiri, X. H. Tan, E. M. Lotfabad, B. C. Olsen, D. Mitlin, *ACS Nano* **2013**, *7*, 11004; d) Y. Yan, Y. X. Yin, Y. G. Guo, L. J. Wan, *Adv. Energy Mater.* **2014**, *4*, 1301584.

[12] a) X. W. Lou, C. M. Li, L. A. Archer, *Adv. Mater.* **2009**, *21*, 2536; b) S. Ding, J. S. Chen, X. W. Lou, *Adv. Funct. Mater.* **2011**, *21*, 4120; c) Z. Wang, L. Zhou, X. W. Lou, *Adv. Mater.* **2012**, *24*, 1903; d) J. S. Chen, X. W. Lou, *Small* **2013**, *9*, 1877.

[13] Y. H. Xu, Y. J. Zhu, Y. H. Liu, C. S. Wang, *Adv. Energy Mater.* **2013**, *3*, 128.

[14] Y. H. Liu, Y. H. Xu, Y. J. Zhu, J. N. Culver, C. A. Lundgren, K. Xu, C. S. Wang, *ACS Nano* **2013**, *7*, 3627.

[15] H. L. Zhu, Z. Jia, Y. C. Chen, N. Weadock, J. Y. Wan, O. Vaaland, X. G. Han, T. Li, L. B. Hu, *Nano Lett.* **2013**, *13*, 3093.

[16] a) J. Chen, F. Y. Cheng, *Acc. Chem. Res.* **2009**, *42*, 713; b) G. Derrien, J. Hassoun, S. Panero, B. Scrosait, *Adv. Mater.* **2007**, *19*, 2336; c) J. Hassoun, G. Derrien, S. Panero, B. Scrosait, *Adv. Mater.* **2008**, *20*, 3169.

[17] Y. H. Xu, Q. Liu, Y. J. Zhu, Y. H. Liu, A. Langrock, M. R. Zachariah, C. S. Wang, *Nano Lett.* **2013**, *13*, 470.

[18] Z. Q. Zhu, S. W. Wang, J. Du, Q. Jin, T. R. Zhang, F. Y. Cheng, J. Chen, *Nano Lett.* **2014**, *14*, 153.

[19] N. Zhang, Q. Zhao, X. P. Han, J. G. Yang, J. Chen, *Nanoscale* **2014**, *6*, 2827.

[20] J. Guo, Z. Yang, L. A. Archer, *J. Mater. Chem. A* **2013**, *1*, 8710.

[21] Y. L. Liang, R. J. Feng, S. Q. Yang, H. Ma, J. Liang, J. Chen, *Adv. Mater.* **2011**, *23*, 640.

[22] X. G. Han, Y. Liu, Z. Jia, Y. C. Chen, J. Y. Wan, N. Weadock, K. J. Gaskell, T. Li, L. B. Hu, *Nano Lett.* **2014**, *14*, 139.

[23] B. Luo, B. Wang, X. L. Li, Y. Y. Jia, M. H. Liang, L. J. Zhi, *Adv. Mater.* **2012**, *24*, 3538.

[24] J. W. Wang, X. H. Liu, S. X. Mao, J. Y. Huang, *Nano Lett.* **2012**, *12*, 5897.

[25] Q. Li, X. F. Lu, H. Xu, Y. X. Tong, G. R. Li, *ACS Appl. Mater. Interfaces* **2014**, *6*, 2726.

[26] Y. M. Lin, P. R. Abel, A. Gupta, J. B. Goodenough, A. Heller, C. B. Mullins, *ACS Appl. Mater. Interfaces* **2013**, *5*, 8273.

[27] S. Komaba, Y. Matsuura, T. Ishikawa, N. Yabuuchi, W. Mutata, S. Kuze, *Electrochem. Commun.* **2012**, *21*, 65.

[28] M. K. Datta, R. Epur, P. Saha, K. Kadakia, S. K. Park, P. N. Kumta, *J. Power Sources* **2013**, *225*, 316.